Li, X., Zus, F., Lu, C., Dick, G., Ning, T., Ge, M., Wickert, J., Schuh, H. (2015): Retrieving of atmospheric parameters from multi-GNSS in real time: Validation with water vapor radiometer and numerical weather model. - *Journal of Geophysical Research*, *120*, 14, p. 7189-7204.

DOI: http://doi.org/10.1002/2015JD023454

AGU PUBLICATIONS

JGR

Journal of Geophysical Research: Atmospheres

RESEARCH ARTICLE
10.1002/2015JD023454

Key Points:
- Atmospheric parameters are retrieved in real time from multi-GNSS observations
- Multi-GNSS improves single-system solution of accuracy, robustness, and coverage
- Such products might be valuable for atmospheric sounding systems and nowcasting

Correspondence to:
F. Zus,
zusflo@gfz-potsdam.de

Citation:
Li, X., F. Zus, C. Lu, G. Dick, T. Ning, M. Ge, J. Wickert, and H. Schuh (2015), Retrieving of atmospheric parameters from multi-GNSS in real time: Validation with water vapor radiometer and numerical weather model, *J. Geophys. Res. Atmos.*, *120*, 7189–7204, doi:10.1002/2015JD023454.

Received 31 MAR 2015
Accepted 28 JUN 2015
Accepted article online 1 JUL 2015
Published online 29 JUL 2015

Retrieving of atmospheric parameters from multi-GNSS in real time: Validation with water vapor radiometer and numerical weather model

Xingxing Li[1,2], Florian Zus[1], Cuixian Lu[1,2], Galina Dick[1], Tong Ning[1], Maorong Ge[1], Jens Wickert[1], and Harald Schuh[1]

[1]German Research Centre for Geosciences GFZ, Potsdam, Germany, [2]School of geodesy and geomatics, Wuhan University, Wuhan, China

Abstract The multiconstellation Global Navigation Satellite Systems (GNSS) (e.g., GPS, GLObal NAvigation Satellite System (GLONASS), Galileo, and BeiDou) offers great opportunities for real-time retrieval of atmospheric parameters for supporting numerical weather prediction nowcasting or severe weather event monitoring. In this study, the observations from different GNSS are combined to retrieve atmospheric parameters based on the real-time precise point positioning technique. The atmospheric parameters, retrieved from multi-GNSS observations of a 180 day period from about 100 globally distributed stations, including zenith total delay, integrated water vapor, horizontal gradient, and slant total delay (STD), are analyzed and evaluated. The water vapor radiometer data and a numerical weather model, the operational analysis of the European Centre for Medium-Range Weather Forecasts (ECMWF), are used to independently validate the performance of individual GNSS and also demonstrate the benefits of multiconstellation GNSS for real-time atmospheric monitoring. Our results show that the GLONASS and BeiDou have the potential capability for real-time atmospheric parameter retrieval for time-critical meteorological applications as GPS does, and the combination of multi-GNSS observations can improve the performance of a single-system solution in meteorological applications with higher accuracy and robustness. The multi-GNSS processing greatly increases the number of STDs. The mean and standard deviation of STDs between each GNSS and ECMWF exhibit a good stability as function of the elevation angle, the azimuth angle, and time, in general. An obvious latitude dependence is confirmed by a map of station specific mean and standard deviations. Such real-time atmospheric products, provided by multi-GNSS processing with higher accuracy, stronger reliability, and better distribution, might be highly valuable for atmospheric sounding systems, especially for nowcasting of extreme weather.

1. Introduction

GPS meteorology, using ground GPS receivers for sounding of atmospheric water vapor, was first proposed by *Bevis et al.* [1992]. Since then, it was tremendously developed, and the related data products are widely used in atmospheric research and by numerical weather prediction (NWP) centers. The GPS technique has significant advantages compared to traditional atmospheric sounding techniques, including low operating expense, all-weather operability, high temporal resolution, and spatial coverage [*Rocken et al.*, 1993, 1997; *Ware et al.*, 1997; *Fang et al.*, 1998; *Dick et al.*, 2001; *Gendt et al.*, 2004; *Mattioli et al.*, 2005]. GPS-based tropospheric data products, including zenith total delays (ZTD) and integrated water vapor (IWV), derived in near real time are currently continuously assimilated into numerical weather prediction models [*Karabatic et al.*, 2011; *Dousa and Vaclavovic*, 2014], and the benefit of GPS-derived tropospheric products on NWP has also been demonstrated [e.g., *Gutman et al.*, 2004; *Haan et al.*, 2004; *Shoji et al.*, 2011].

In the recent years, some innovative applications such as nowcasting of severe weather events or regional short-term forecast systems require more rapid updates of the atmospheric state with short or no latency. Therefore, the development of real-time tropospheric products is one of the main topics within the new European Coordination in Science and Technology Action ES1206 "Advanced Global Navigation Satellite Systems tropospheric products for monitoring severe weather events and climate (GNSS4SWEC)," which started in May 2013 with 33 participating countries (http://www.cost.eu/domains_actions/essem/Actions/ES1206). Especially, the International GNSS Service (IGS) real-time service [*Caissy et al.*, 2012] enables real-time precise point positioning (PPP) [*Zumberge et al.*, 1997; *Li et al.*, 2013a] based water vapor retrieval for tropospheric

monitoring [*Li et al.*, 2014; *Dousa and Vaclavovic*, 2014; *Yuan et al.*, 2014]. Compared to the baseline/network approach, the single-receiver PPP approach has higher efficiency and better flexibility and is especially suitable for the real-time analysis of dense GPS networks with a large number of stations [*Li et al.*, 2013b].

Nowadays, the world of satellite navigation is undergoing dramatic changes. In addition to GPS and the recovered Russia's Global Navigation Satellite System (GLONASS), the new and emerging satellite navigation systems China's BeiDou and European Union's Galileo provide the potential for extended, more accurate, and more reliable GNSS applications [*Rizos et al.*, 2013; *Li et al.*, 2015a]. Currently (as of end 2014), about 74 navigation satellites are already in orbit and transmit signals—about 120 will be available once all four systems (i.e., GPS, GLONASS, Galileo, and BeiDou) are fully operated. Accordingly, the IGS has initiated the Multi-GNSS Experiment (MGEX) to acquire and analyze data from all four constellations. As a backbone of the MGEX project, a new network of multi-GNSS monitoring ground stations has been globally deployed over the past 2 years [*Montenbruck et al.*, 2014]. The MGEX network has grown to more than 100 stations now, and it provides an excellent opportunity to demonstrate the potential benefits from multiconstellation GNSS.

In view of the increased number of transmitting satellites, more tropospheric slant total delays (STD) are available in parallel and the ZTD/gradient parameter estimation will benefit from an improved spatial distribution of observations tracked by the ground-based receivers for more accurate and robust tropospheric monitoring. Especially, it would be beneficial in case of blocked satellites [*Al-Shaery et al.*, 2013; *Li et al.*, 2015a]. In this contribution, we combine GPS, GLONASS, Galileo, and BeiDou observations together for real-time tropospheric monitoring based on the PPP approach. The multi-GNSS observations from about 100 globally distributed stations are processed, and measurements from water vapor radiometer (WVR) and a numerical weather model are used for independent validation of the derived atmospheric GNSS data products. The retrieved parameters, as ZTD, IWV, horizontal gradient, and STD, are analyzed to evaluate the performance of each constellation and also to validate the contribution of multi-GNSS joint processing to the atmospheric parameters.

2. Real-Time Retrieving Atmospheric Parameters From Multi-GNSS

The GNSS phase $L^s_{r,j}$ and pseudorange $P^s_{r,j}$ observation equations can be expressed as following [*Li et al.*, 2011],

$$L^s_{r,j} = \rho^s_r g - t^s + t_r + \lambda_j\left(b_{r,j} - b_j{}^s\right) + \lambda_j N^s_{r,j} - I^s_{r,j} + T^s_r + \varepsilon^s_{r,j} \tag{1}$$

$$P^s_{r,j} = \rho^s_r g - t^s + t_r + c\left(d_{r,j} - d_j{}^s\right) + I^s_{r,j} + T^s_r + e^s_{r,j} \tag{2}$$

where s, r, and j refer to satellite, receiver, and frequency, respectively; t^s and t_r are the clock biases; $N^s_{r,j}$ is the integer ambiguity; $b_{r,j}$ and $b_j{}^s$ are the uncalibrated phase delays; λ_j is the wavelength; $d_{r,j}$ and $d_j{}^s$ are the code biases; the ionospheric delays $I^s_{r,j}$ at different frequencies can be expressed as $I^s_{r,j} = \kappa_j \cdot I^s_{r,1},\ \kappa_j = \lambda_j{}^2/\lambda_1{}^2$; T^s_r is the slant tropospheric delay; $e^s_{r,j}$ and $\varepsilon^s_{r,j}$ denote the sum of measurement noise and multipath error for the pseudorange and carrier phase observations; and ρ_g denotes the geometric distance. The phase center offsets and variations, tidal loading, and phase wind-up can be corrected according to the existing models [*Kouba*, 2009]. Under the multiconstellation environment, the combined GPS + GLONASS + Galileo + BeiDou observation model can be formulated as

$$\begin{cases} L^G_{r,j} = \rho^G_r g - t^G + t_r + \lambda_{jG}\left(b_{rG,j} - b_j{}^G\right) + \lambda_{jG} N^G_{r,j} - \kappa_{jG} \cdot I^G_{r,1} + T^G_r + \varepsilon^G_{r,j} \\ L^{R_k}_{r,j} = \rho^R_r g - t^R + t_r + \lambda_{jR_k}\left(b_{rR_k,j} - b_j{}^R\right) + \lambda_{jR_k} N^R_{r,j} - \kappa_{jR_k} \cdot I^R_{r,1} + T^R_r + \varepsilon^R_{r,j} \\ L^E_{r,j} = \rho^E_r g - t^E + t_r + \lambda_{jE}\left(b_{rE,j} - b_j{}^E\right) + \lambda_{jE} N^E_{r,j} - \kappa_{jE} \cdot I^E_{r,1} + T^E_r + \varepsilon^E_{r,j} \\ L^C_{r,j} = \rho^C_r g - t^C + t_r + \lambda_{jC}\left(b_{rC,j} - b_j{}^C\right) + \lambda_{jC} N^C_{r,j} - \kappa_{jC} \cdot I^C_{r,1} + T^C_r + \varepsilon^C_{r,j} \end{cases} \tag{3}$$

$$\begin{cases} P^G_{r,j} = \rho^G_r g - t^G + t_r + c\left(d_{rG,j} - d_j{}^G\right) + \kappa_{jG} \cdot I^G_{r,1} + T^G_r + e^G_{r,j} \\ P^{R_k}_{r,j} = \rho^R_r g - t^R + t_r + c\left(d_{rR_k,j} - d_j{}^R\right) + \kappa_{jR_k} \cdot I^R_{r,1} + T^R_r + e^R_{r,j} \\ P^E_{r,j} = \rho^E_r g - t^E + t_r + c\left(d_{rE,j} - d_j{}^E\right) + \kappa_{jE} \cdot I^E_{r,1} + T^E_r + e^E_{r,j} \\ P^C_{r,j} = \rho^C_r g - t^C + t_r + c\left(d_{rC,j} - d_j{}^C\right) + \kappa_{jC} \cdot I^C_{r,1} + T^C_r + e^C_{r,j} \end{cases} \tag{4}$$

where the indices G, R, E, and C refer to the GPS, GLONASS, Galileo, and BeiDou satellites, respectively, and R_k denotes the GLONASS satellite with frequency factor k. Due to the different frequencies and signal structure

of the individual GNSS, the code bias d_{rG}, d_{rR_k}, d_{rE}, and d_{rC} are different in one multi-GNSS receiver. The differences between them are called intersystem biases (ISB). For the GLONASS satellites with different frequency factors, the receiver code biases d_{rR_k} are also different and called interfrequency biases (IFB). The intersystem and interfrequency biases must be considered in a combined processing of multi-GNSS observations. We setup the code bias parameters for each system and each GLONASS frequency. The code bias for GPS satellites is set to zero in order to eliminate the singularity between receiver clock and code bias parameters. This means that all estimated biases of other systems are relative to the biases for the GPS satellites.

For the real-time PPP processing, precise satellite orbits and clocks have to be first determined using the observation data from a global GNSS ground tracking network. Similar to the procedure of the IGS ultrarapid orbits, the real-time orbit is predicted (here 6 h prediction) based on the orbits determined in a batch-processing mode by using an orbit integrator. With fixed satellite orbits and station coordinates, satellite clocks are then estimated and updated epoch by epoch due to its short-term fluctuations [*Zhang et al.*, 2012]. It is worthwhile to note that zero mean conditions over the ISB/IFB parameters need to be introduced for each system (i.e., BeiDou and Galileo) and each GLONASS frequency in the multi-GNSS orbit and clock determination [*Dach et al.*, 2006]. The station coordinates are usually well known in meteorological applications. When the real-time orbit and clock corrections are available [*Li et al.*, 2015b], the multi-PPP model can be simplified as

$$\begin{cases} I_{r,j}^{G} = t_r + \lambda_{jG}\left(b_{rG,j} - b_j^{G}\right) + \lambda_{jG}N_{r,j}^{G} - \kappa_{jG}\cdot I_{r,1}^{G} + T_r^{G} + \varepsilon_{r,j}^{G} \\ I_{r,j}^{R_k} = t_r + \lambda_{jR_k}\left(b_{rR_k,j} - b_j^{R}\right) + \lambda_{jR_k}N_{r,j}^{R} - \kappa_{jR_k}\cdot I_{r,1}^{R} + T_r^{R} + \varepsilon_{r,j}^{R} \\ I_{r,j}^{E} = t_r + \lambda_{jE}\left(b_{rE,j} - b_j^{E}\right) + \lambda_{jE}N_{r,j}^{E} - \kappa_{jE}\cdot I_{r,1}^{E} + T_r^{E} + \varepsilon_{r,j}^{E} \\ I_{r,j}^{C} = t_r + \lambda_{jC}\left(b_{rC,j} - b_j^{C}\right) + \lambda_{jC}N_{r,j}^{C} - \kappa_{jC}\cdot I_{r,1}^{C} + T_r^{C} + \varepsilon_{r,j}^{C} \end{cases} \tag{5}$$

$$\begin{cases} p_{r,j}^{G} = t_r + c{\cdot}d_{rG} + \kappa_{jG}\cdot I_{r,1}^{G} + T_r^{G} + e_{r,j}^{G} \\ p_{r,j}^{R_k} = t_r + c\cdot d_{rR_k} + \kappa_{jR_k}\cdot I_{r,1}^{R} + T_r^{R} + e_{r,j}^{R} \\ p_{r,j}^{E} = t_r + c\cdot d_{rE} + \kappa_{jE}\cdot I_{r,1}^{E} + T_r^{E} + e_{r,j}^{E} \\ p_{r,j}^{C} = t_r + c\cdot d_{rC} + \kappa_{jC}\cdot I_{r,1}^{C} + T_r^{C} + e_{r,j}^{C} \end{cases} \tag{6}$$

where $I_{r,j}^{s}$ and $p_{r,j}^{s}$ denote "observed minus computed" phase and pseudorange observables. The slant tropospheric delay T_r^s consists of the hydrostatic and wet components and both can be expressed by their individual zenith delay and mapping function:

$$T_r^s = \mathrm{Mh}_r^s\cdot \mathrm{Zh}_r + \mathrm{Mw}_r^s\cdot\left[\mathrm{Zw}_r + \cot(e)\cdot\left(G_N\cdot\cos(a) + G_E\cdot\sin(a)\right)\right] \tag{7}$$

The zenith hydrostatic delay (ZHD) Zh_r can be computed rather accurately using the Saastamoinen model [*Saastamoinen*, 1973] and meteorological data; the zenith wet delay (ZWD) Zw_r and horizontal gradients (G_N and G_E are the gradients in north and east directions) have to be estimated as parameters [*Li et al.*, 2015c]. Mh_r^s and Mw_r^s are the hydrostatic and wet coefficients of the global mapping function (GMF) [*Böhm et al.*, 2006]; e and a are the elevation and azimuth angle.

In our multi-GNSS PPP-based atmospheric parameter retrieving, the estimated parameters vector $\mathbf{X}$ can be expressed as

$$\mathbf{X} = \left(\mathrm{Zw}_r\ G_N\ G_E\ t_r\ d_{rE}\ d_{rC}\ d_{rR_k}\ \mathbf{I}_{r,1}^{s}\ \overline{\mathbf{N}}_r^{s}\right)^{T} \tag{8}$$

$$\overline{\mathbf{N}}_r^{s} = \mathbf{N}_r^{s} + \mathbf{b}_r + \mathbf{b}^{s} \tag{9}$$

A sequential least squares filter is employed to estimate the unknown parameters in real-time processing. All the observations from different GNSS (four systems) are processed together in one common estimator to perform a rigorous multi-GNSS analysis with careful consideration of intersystem and interfrequency biases. The receiver clock bias t_r is estimated epoch-wise as white noise. The ISB and IFB parameters are estimated as constant over time (one processed day), and GPS is selected as reference. The phase delays b_r and b^s will be absorbed by phase ambiguity parameters, and the phase ambiguities $\overline{\mathbf{N}}_r^{s}$ are estimated as constant for each continuous arc. The ionospheric delays $\mathbf{I}_{r,1}^{s}$ are taken as estimated parameters for each satellite and at each epoch by using dual-frequency raw phase and pseudorange observations. The tropospheric

Table 1. Multi-GNSS Data Processing Strategy for Real-Time Atmospheric Parameter Retrieving

Item	Strategies
Estimator	All the multi-GNSS observations are processed together in one common least squares estimator
Observations	Raw carrier phase and pseudorange observations; GPS + GLONASS + BeiDou + Galileo, 74 navigation satellites
Signal selection	GPS: L1/L2; GLONASS: L1/L2; BeiDou: B1/B2; Galileo: E1/E5a
Sampling rate	30 s
Elevation cutoff	7°
Weight for observations	The variance component estimation weighting method
Satellite orbit	Fixed
Satellite clock	Fixed
Zenith tropospheric delay	Initial model + random-walk process
Tropospheric gradients	Estimated every 12 h
Mapping function	Global mapping function (GMF)
Phase-windup effect	Corrected
Receiver clock	Estimated, white noise
ISB and IFB	Estimated as constant, GPS as reference
Station displacement	Solid Earth tide, pole tide, ocean tide loading International Earth Rotation Service Convention 2010
Satellite antenna phase center	Corrected using MGEX and IGS values
Receiver antenna phase center	Corrected
Station coordinate	Fixed to weekly solution
Phase ambiguities	Constant for each continuous arc, without ambiguity resolution

ZWD Zw_r is modeled as a random walk process, and the noise intensity is about 5–10 $mm/\sqrt{hour}$. The horizontal delay gradient parameters in north and east directions are estimated in intervals of 12 h. The variance component estimation weighting method is applied. Table 1 summarizes our multi-GNSS data processing strategy for real-time atmospheric parameter retrieving.

With the ZHD Zh_r and the estimated tropospheric parameters Zw_r, G_N and G_E, the STD can be reconstructed according to

$$\widetilde{T}_r^s = \mathrm{Mh}_r^s \cdot \mathrm{Zh}_r + \mathrm{Mw}_r^s \cdot [\mathrm{Zw}_r + \cot(e) \cdot (G_N \cdot \cos(a) + G_E \cdot \sin(a))] + R \tag{10}$$

where $\widetilde{T}_r^s$ is the reconstructed STD, R denotes the postfit phase residual, in which residual tropospheric delays are included.

Meanwhile, Zw_r can be converted to the IWV once it is accurately estimated [*Askne and Nordius*, 1987],

$$\mathrm{IWV} = \Pi(T_m) \cdot \mathrm{Zw} \tag{11}$$

$$\Pi(T_m) = \frac{10^6}{\rho_w R_v \left(\frac{k_3}{T_m} + k_2^{'}\right)} \tag{12}$$

where ρ_w (999.97 kg m^{-3}) denotes the density of liquid water, R_v (461.51 $JK^{-1}kg^{-1}$) is the specific gas constant of water vapor, k_3 and $k_2^{'}$ are the atmospheric refraction constants ($k_2^{'} = 22.1 \pm 2.2 (\mathrm{K\ hPa}^{-1})$, $k_3 = 373900 \pm 1200 (\mathrm{K^2 hPa}^{-1})$). The $\Pi(T_m)$ depends on the atmospheric mean temperature T_m, and its value is typically around 0.15 but can vary up to 15%. The T_m can be calculated utilizing the temperature data from the European Centre for Medium-Range Weather Forecasts (ECMWF) analysis [*Bevis et al*., 1994; *Wang et al*., 2005].

In this study, pressure provided by the Global Pressure and Temperature 2 [*Lagler et al*., 2013] model is used to calculate the a priori ZHD so as to derive the ZTD (PPP-derived ZTD). However, the remaining error in ZHD will be absorbed into the estimated ZWD during parameter estimation if the a priori ZHD is not accurate enough. Consequently, the error will also propagate to the converted IWV. Accurate surface pressure values from meteorological sensors can be used for accurate modeling of ZHD, but they are usually not available for most of the stations. Therefore, for any station, we use the pressure data from the ECMWF analysis to calculate a new more accurate ZHD, and then the accurate ZWD can be obtained by subtracting the accurately new ZHD from the PPP-derived ZTD. Finally, the new ZWD is converted into IWV using equation (11) and (12).

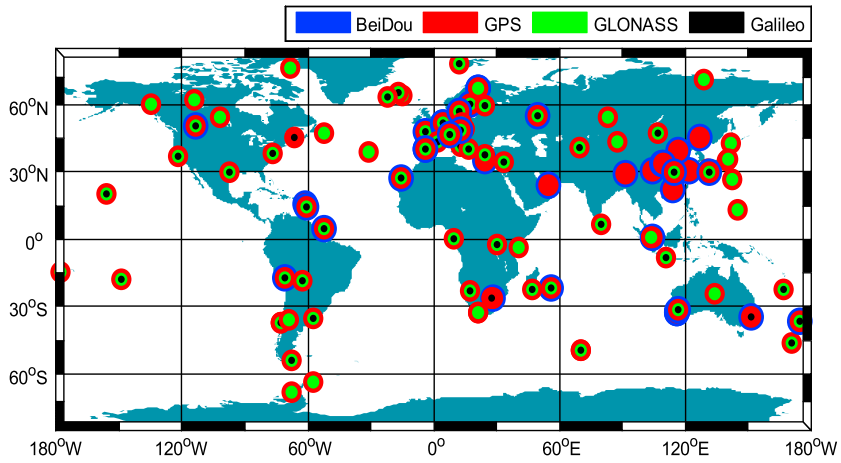

Figure 1. The distribution of multi-GNSS stations from MGEX and BETN networks. Their supported constellations are shown in different colors, BeiDou in blue, GPS in red, GLONASS in green, and Galileo in black.

3. Multitechnique Data Collection

3.1. Multi-GNSS Data

Currently (as of end 2014) 32 GPS satellites and 24 GLONASS satellites are in orbit. Meanwhile, the Galileo and BeiDou systems, which are still under development, consist of 4 and 14 satellites, respectively. In response to the upcoming new signals and systems, the MGEX has been set up by the IGS to track, collect, and analyze all available GNSS signals of interest. Currently about 27 contributing agencies from 16 countries are involved in this project [http://igs.org/mgex, *Montenbruck et al.*, 2014]. As a backbone of the MGEX project, a new network of multi-GNSS monitoring stations has been deployed in parallel to the legacy IGS network for GPS and GLONASS since 2012. Today, it comprises over 110 stations around the world, most of them enable real-time data access in addition to off-line archival data. As a minimum, all MGEX stations support tracking of GPS as well as at least one of the new Galileo or BeiDou constellations.

The BeiDou experimental tracking network (BETN) established by Wuhan University is a continuous global observation reference network. Since 2011, nine tracking stations in China and seven tracking stations outside of China have been included in BETN [*Ge et al.*, 2012]. All the stations are equipped with the UB240-CORS GPS/BeiDou dual-system receivers and the UA240 antennas manufactured by the UNICORE Company, China. Figure 1 shows an overview of the buildup MGEX and BETN stations and their supported constellations. These multi-GNSS data provide an excellent opportunity for our study.

3.2. Water Vapor Radiometer Data

The Onsala Space Observatory is operating a WVR, which carries out measurements in a dual-frequency (21.0 and 31.4 GHz) and is mounted less than 10 m away from the four-system MGEX station, ONS1 with a height difference less than 1 m. The WVR is operated continuously in a so-called "sky-mapping" mode, which corresponds to a repeated cycle (every 15 min) of 60 observations spread over the sky with the lowest elevation angle of 20°, typically resulting in 6000–9000 measurements per day. The WVR wet delays were inferred from the sky brightness temperatures using tip curves for calibration as described by *Elgered and Jarlemark* [1998]. The IWV data products from this WVR are used as independent measurements to validate the GNSS-derived IWV estimates in this study.

3.3. ECMWF Data

Given Numerical Weather Model data and a point-to-point ray-trace algorithm, STDs (and ZTDs) can be computed for any station-satellite link [see, e.g., *Zus et al.*, 2012]. The numerical weather model (NWM) has the advantage to analyze the GNSS-derived ZTD and STD at any station. We use the ray-trace algorithm proposed by *Zus et al.* [2014] and the pressure, temperature, and specific humidity data from the operational analysis of the ECMWF (http://www.ecmwf.int/). Gradients are estimated from the STDs by a least squares fit similar to equation (7) [*Zus et al.*, 2015]. The ECMWF analysis data at the

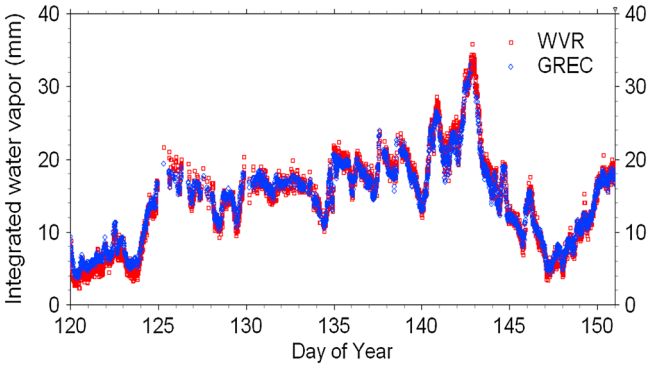

Figure 2. IWV results derived from multi-GNSS (G + R + E + C) PPP and WVR at station ONS1 (Sweden and Europe) from day of year 121 to 151 in 2014. The four-system combined solutions are shown by the blue symbols, while the WVR-derived IWV are shown by the red symbols.

GFZ are available with a horizontal resolution of 1° × 1° on 137 model levels extending from Earth's surface to about 80 km. Since the ECMWF analysis is solely available every 6 h and we do not interpolate in time, we restrict the comparison of GNSS and ECMWF STDs (ZTDs and gradients) to the analysis times 00:00, 06:00, 12:00, and 18:00 UTC.

4. Results and Validations

All the MGEX and BETN data during the first half year of 2014 are processed in real-time PPP mode to generate ZTD, IWV, gradients, and STD as described in section 2. The results are compared to the collocated WVR and also ECMWF derived STDs as independent evaluations in this section.

4.1. IWV Validation With WVR Data

Among the multi-GNSS stations, the four-system MGEX station ONS1 has a collocated WVR and the water vapor data are available for our study. The IWV series derived from multi-GNSS ($G+R+E+C$) PPP and WVR at the ONS1 (Sweden and Europe) for May 2014 (day of year (DOY) 121–151) are shown in Figure 2. The four-system combined solutions are shown by the blue symbols, while the WVR-derived IWV are shown by the red symbols. The comparison shows that the four-system combined IWV agrees quite well with the WVR-derived IWV, in general, except some outliers in WVR results. Figure 3 shows the linear correlation between the multi-GNSS IWV and WVR-derived IWV at ONS1. The multi-GNSS IWV can be very well fitted by the WVR-derived IWV. The correlation coefficient between them is 0.98, which indicates a rather high correlation.

Figure 4 shows the IWV differences between the GNSS solutions and WVR measurements at the station ONS1 during the corresponding period. The differences between the four-system combined solution and WVR data (shown by the blue symbols) are, in general, smaller than 3.0 mm, and the statistical root-mean-square (RMS) value is 1.2 mm. The difference series for the GPS-only, GLONASS-only, and BeiDou-only solutions are also shown in the same figure by the red, green, and black symbols, respectively. The Galileo-only solution is not available as too few (four at the moment) satellites are in the sky, and it cannot provide autonomous application. The systematic trend, which is visible in all the GNSS solutions, may be from the WVR-derived IWV estimates.

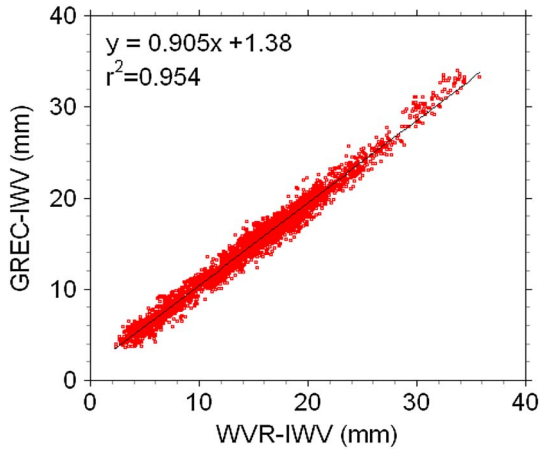

Figure 3. Linear correlation of multi-GNSS IWV to WVR-derived IWV at station ONS1 (Sweden and Europe). The regression line and the r^2 coefficient are also depicted.

We can see that the combined solution provides the smallest bias to the WVR data, while the BeiDou-only solution reveals the largest ones. The GLONASS-only solution is slightly worse than the GPS-only solution, and the RMS values for them are 1.8 and 1.6 mm, respectively. The BeiDou-derived IWV presents larger noise and more outliers, the RMS value is about 2.5 mm. The reason is that only 4–7 BeiDou satellites can be observed at this location due to BeiDou's current constellation, including four Medium Earth Orbits, five Inclined Geosynchronous Orbits, and five Geosynchronous Orbits, to guarantee sufficient visible satellites in the Asia-Pacific area.

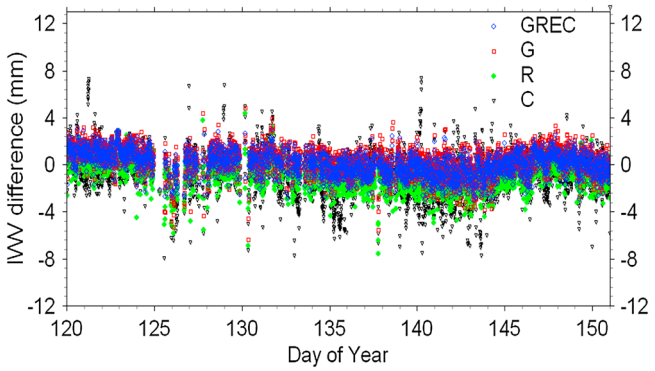

Figure 4. The IWV differences between GNSS solutions and WVR solution at station ONS1 (Sweden and Europe) from day of year 120 to 151 in 2014. The difference series for four-system combined solution are shown by the blue symbols, and the difference series for GPS-only, GLONASS-only, and BeiDou-only solutions are shown by the red, green, and black symbols, respectively.

Therefore, only a limited number can be observed in some regions such as Europe. This situation is expected to be improved when the BeiDou constellation is fully completed. It can be found that there are some outliers in single-system solutions. Although the GPS- and GLONASS-derived IWV are stable and have much less outliers than BeiDou-derived IWV, there are still some outliers visible. The reason is that only few observations are available or data quality problems in some cases. These outliers, appearing in single-system solutions, can be solved when multi-GNSS observations are processed simultaneously. The distribution of the IWV differences between the GNSS solutions and the WVR solution is shown in Figure 5.

From the comparisons, we can conclude that the GLONASS and BeiDou also have the potential capability for real-time IWV retrieval for time-critical meteorological applications such as NWP nowcasting and severe weather event monitoring as GPS does. The combination of multi-GNSS observations can improve the performance of single-system solution in meteorological applications with higher accuracy and robustness.

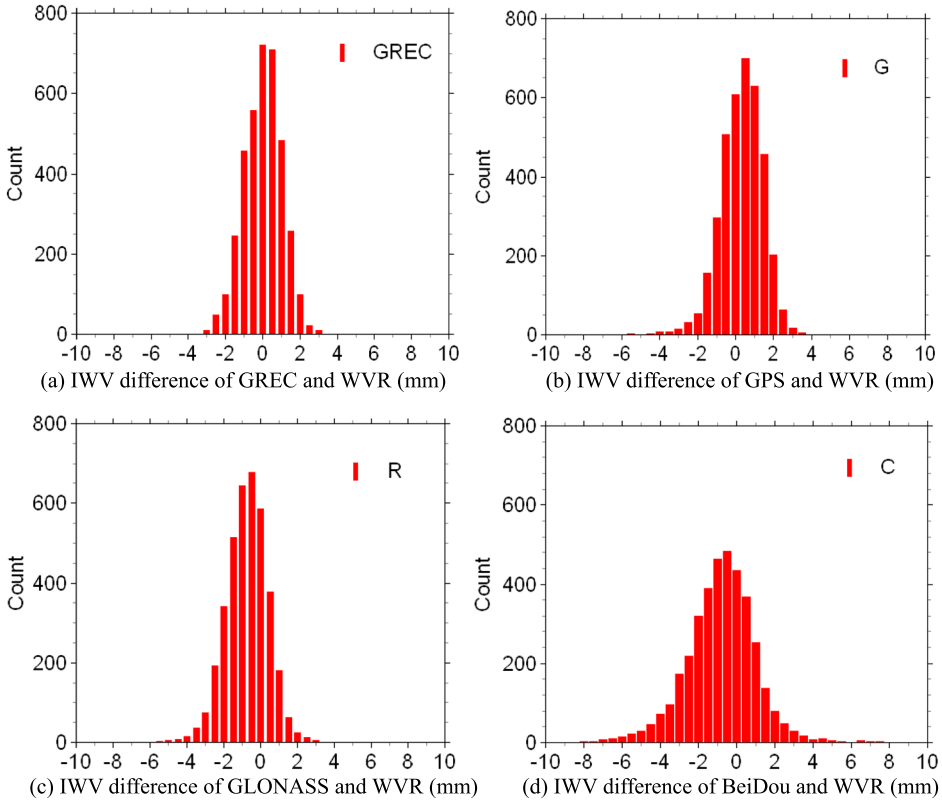

Figure 5. The distribution of the IWV differences between GNSS solutions and WVR solution at ONS1. (a) The distribution for multi-GNSS combined solution. (b) The distribution for GPS-only solution. (c) The distribution for GLONASS-only solution. (d) The distribution for BeiDou-only solution.

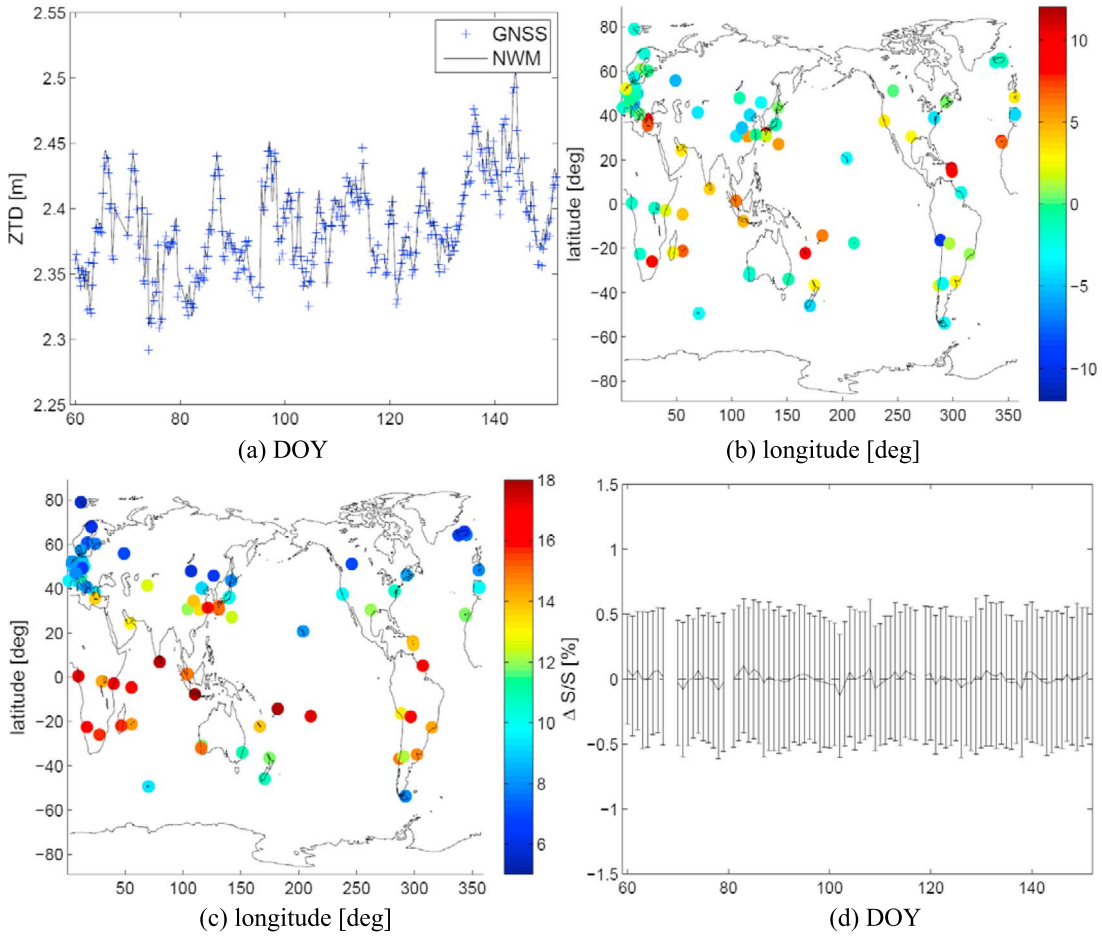

Figure 6. The statistical comparison between multi-GNSS ZTDs and ECMWF ZTDs for the DOY 60–150 in 2014. (a) The ZTD time series derived from multi-GNSS and ECMWF at the station ONS1. (b) The map of station specific mean deviations (c) The map of station specific standard deviation. (d) The fractional deviation as a function of the day of year. The black line indicates the mean deviation, and the error bars indicate the standard deviation from the mean deviation. In total 29392 ZTDs enter the comparison.

4.2. ZTD Validation With ECMWF

The ZTDs derived from multi-GNSS combined solutions are compared to the ECMWF ZTDs at all the MGEX and BETN stations for DOY 60–150 in 2014. In total 29,392 ZTDs enter the comparison. The statistical comparison is summarized in Figure 6. Taking the station ONS1 (Sweden, 57.40°N, 11.93°W) as a typical example, Figure 6a already indicates the good agreement between multi-GNSS and ECMWF ZTDs. Rapid changes in the ZTD time series, which are attributed to rapid changes in the humidity in the vicinity of the considered station, are captured by both the multi-GNSS and ECMWF solution. Figure 6b shows the map of station specific mean deviations. It can be seen that the mean deviations at the high-latitude stations are within ±4 mm, while the mean deviations at the low-latitude stations are typically larger and reach up to ±10 mm. Figure 6c shows the map of station specific standard deviations. Similar to the mean deviations, the standard deviations show a strong latitude dependence. The standard deviations of the high-latitude stations are typically below 10 mm, while the standard deviations at the low-latitude stations are between 10 and 16 mm. Clearly, the deviations between multi-GNSS and ECMWF ZTDs are correlated with the atmospheric humidity content: small (large) deviations in dry (moist) regions. This latitude dependence agrees fairly well with the latitude dependency reported by e.g., *Dousa and Bennitt* [2013], who compared near-real time GPS ZTDs with numerical weather model based ZTDs. They find a latitudinal trend in the standard deviation with values of 4 mm at high latitudes increasing to 20 mm in the tropics. They attribute this latitude dependency to the lack of variability in the numerical weather model-based ZTD in the tropics. We fully agree with their explanation; e.g., deviations between different numerical weather models show a similar latitude dependency, but we cannot rule out that the GNSS-based ZTDs have a larger uncertainty in

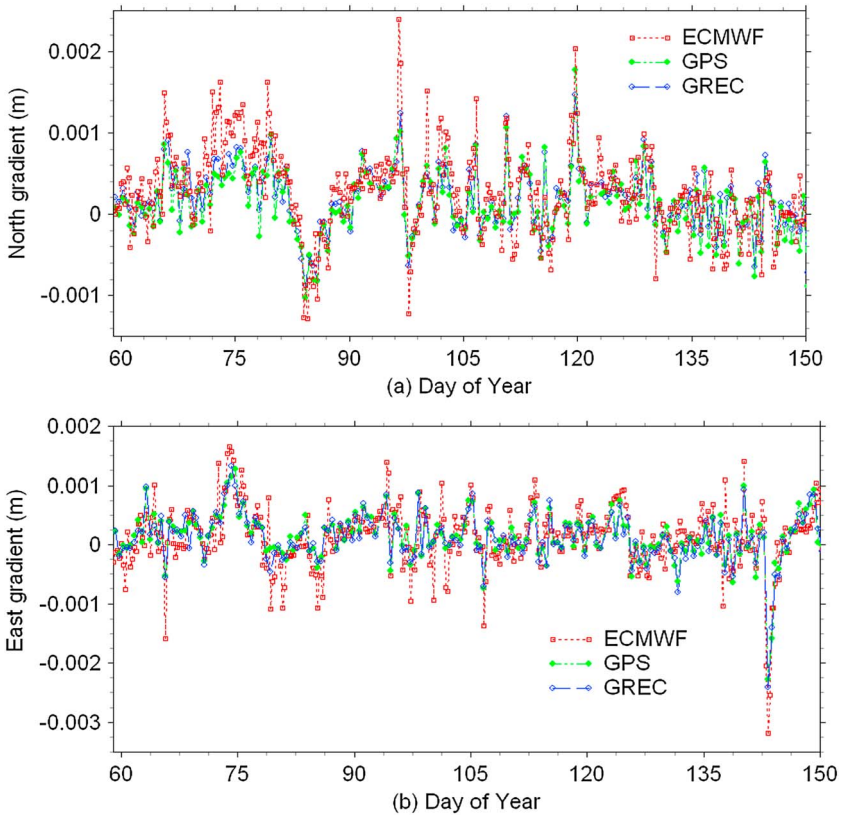

Figure 7. Tropospheric horizontal gradients retrieved from GPS-only and multi-GNSS combined ($G + R + E + C$) solutions at the station ONS1 (57.40°N, 11.93°W, Sweden and Europe) for a period of three months (March, April, and May, day of year 60 to 150 in 2014). The tropospheric gradients derived from ECMWF are used for validation as an independent reference. (a) The north-south gradients of 3 months from GPS-only, multi-GNSS, and ECMWF solutions are shown by the green, blue, and red symbols, respectively. (b) The east-west gradients of three months.

the tropics as well. The fractional deviation between multi-GNSS and ECMWF ZTDs as a function of the day of year shown in Figure 6d indicates the reliability of the multi-GNSS ZTDs; except for few days where no multi-GNSS ZTDs are available, the mean deviations (indicated by the black line) are stable and close to zero (smaller than 0.1%) and the standard deviations (indicated by the error bars) are stable and about 0.5% (with a nominal ZTD of 2.4 m a fractional standard deviation of 0.5% translates into a standard deviation of 12 mm).

4.3. Gradient Evaluation With ECMWF

Taking the multi-GNSS station ONS1 as an example, the tropospheric horizontal gradients retrieved from four-system combined (called as GREC) solutions for a period of 3 months (March, April, and May, day of year 60 to 150 in 2014) are shown in the Figure 7. The tropospheric gradients, derived from ECMWF, are also shown for validation as an independent reference. In the Figure 7a, the north-south gradients of 3 months from multi-GNSS and ECMWF solutions are shown by the blue and red symbols, respectively. It can be found that the multi-GNSS gradients agree well with the ECMWF gradients, which imply that the troposphere gradients can be captured by the multi-GNSS estimates. However, the GNSS-derived gradients were underestimated with respect to the ECMWF gradients, especially for spike-shaped peaks which were mostly associated with synoptic fronts. One has to keep in mind that the gradients from the weather model are a snapshot of the troposphere at a certain epoch, whereas the gradients from the GNSS techniques are averaged over a certain period; e.g., a temporal resolution of 12 h is applied in our processing as usual. Such an averaging process will result in the underestimation of gradient magnitude.

The tropospheric gradients, retrieved from GPS-only solutions, are also shown by the green symbols for the comparison. The multi-GNSS derived gradients agree slightly better with the ECMWF gradients than the

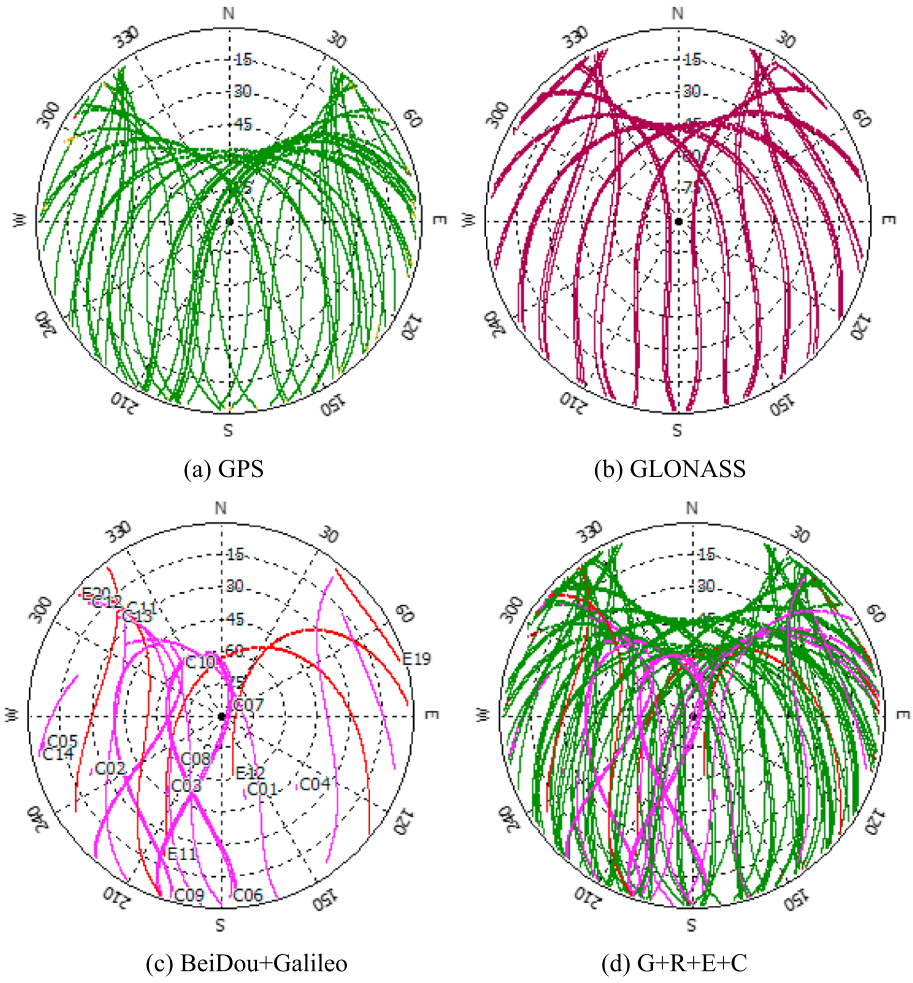

Figure 8. Sky plots (azimuth versus elevation) for GNSS constellations at GMSD. (a) GPS, (b) GLONASS, (c) BeiDou (pink) and Galileo (red), and (d) all the satellites including GPS, GLONASS, BeiDou and Galileo.

GPS-only estimates. We calculated the RMS values of the gradient differences for multi-GNSS and GPS-only solutions with respect to the ECMWF solution, and they are 0.34 and 0.38, respectively. An improvement of about 11.8% is achieved by the multi-GNSS processing. The east gradients of the corresponding 3 months are also compared in Figure 7b. Good agreement between GNSS and ECMWF derived gradients can be observed, although the GNSS-derived gradients are more smooth and have smaller magnitude. The RMS of the east gradient differences between the multi-GNSS and ECMWF solution is 0.35, while the RMS for the GPS-only solution is 0.37, about a 5.7% improvement by multi-GNSS processing. Therefore, we conclude that the multi-GNSS fusion can slightly improve the gradient estimates due to the better observation geometry.

4.4. STD Evaluation With ECMWF

The multi-GNSS processing greatly increase the number of tropospheric slant delays. Taking the station ONS1 as an example, the number of slant delays on is about 25,000, 22,000, 15,000, and 6,000 per day for GPS, GLONASS, BeiDou, and Galileo, respectively. In the four-system solution, the slant delay number can reach up to about 68,000 per day. For the station GMSD (Japan and Asia) located in the Asia-Pacific area, the total number of slant delays will even increase by about 82,000 per day due to better visibility of BeiDou satellites. Figure 8 shows the sky plots (azimuth versus elevation) of GPS, GLONASS, Galileo + BeiDou, and GPS + GLONASS + Galileo + BeiDou at GMSD. Comparing Figure 8d with Figure 8a, we can see that the satellite visibility and spatial geometry are significantly improved under multi-GNSS environment. Such an increase of tropospheric slant delays will also be beneficial for reconstructing the water vapor distribution [*Bender et al.*, 2011].

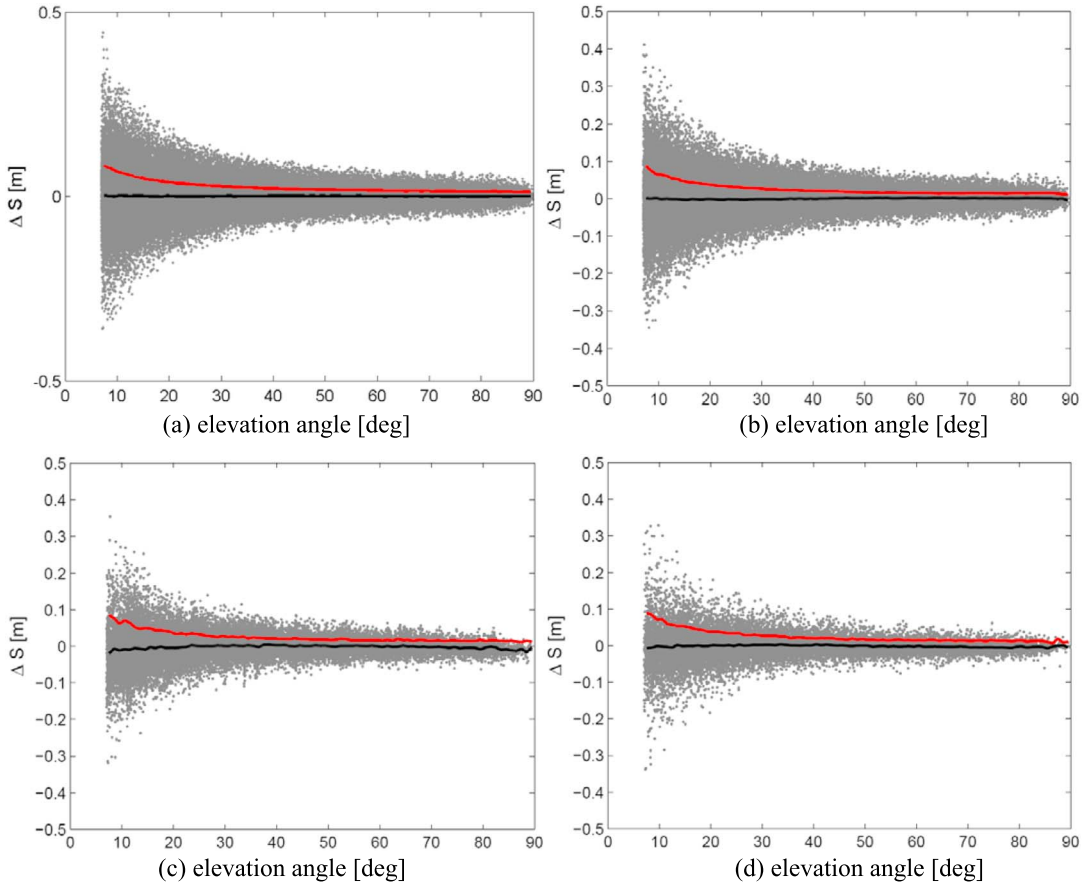

Figure 9. The deviation between GNSS STDs and ECMWF STDs as a function of the elevation angle. The black line indicates the mean deviation, and the red line indicates the standard deviation. The grey dots represent individual STD differences. In total, 487368 STDs enter the comparison, including 244558, 167522, 38237, and 22048 STDs for GPS, GLONASS, BeiDou, and Galileo, respectively. (a) The STD deviation between GPS and ECMWF. (b) The STD deviation between GLONASS and ECMWF. (c) The STD deviation between BeiDou and ECMWF. (d) The STD deviation between Galileo and ECMWF.

Since STDs show a strong elevation angle dependency (the lower the elevation angles, the larger the signal travel time delays induced by the atmosphere), it is convenient to plot the differences between GNSS and ECMWF STDs as a function of the elevation angle. In Figure 9 the grey dots represent individual STD differences. Figures 9a–9d are for GPS, GLONASS, BeiDou, and Galileo, respectively. In total, 487,368 STDs enter the comparison, including 244,558, 167,522, 38,237, and 22,048 STDs for GPS, GLONASS, BeiDou and Galileo, respectively. The black line indicates the mean deviation, and the red line indicates the standard deviation. For any GNSS the mean deviation shows almost no elevation angle dependency. However, the variation of the mean deviation around zero for BeiDou and Galileo is larger than for GPS and GLONASS. At this point (also see discussion below) we attribute this to the error models for the new satellite systems (e.g., the phase center offset (PCO) and phase center variation (PCV) models). Unlike the mean deviation, the standard deviation for any GNSS shows an elevation angle dependency; the standard deviation is about 1 cm close to the zenith and about 10 cm at an elevation angle of 7°. This elevation angle dependency for the standard deviation between GNSS and ECMWF STDs is expected since the STDs and their uncertainties depend on the elevation angle as well.

Therefore, we show in Figure 10 the corresponding fractional deviation between GNSS and ECMWF STDs as a function of the elevation angle (Figure 10, left column) and azimuth angle (Figure 10, right column). Figures 10a–10e are for GPS, GLONASS, BeiDou, Galileo, and multi-GNSS combined STDs. For GPS and GLONASS the mean fractional deviation, indicated by the black line, is close to zero for any elevation angle. However, for BeiDou and Galileo the mean fractional deviation close to the zenith tends to be negative. Compared to GPS and GLONASS, the sample sizes for BeiDou and Galileo are small, but we think that the number of observations is sufficient to allow a statistical interpretation. Specifically, for

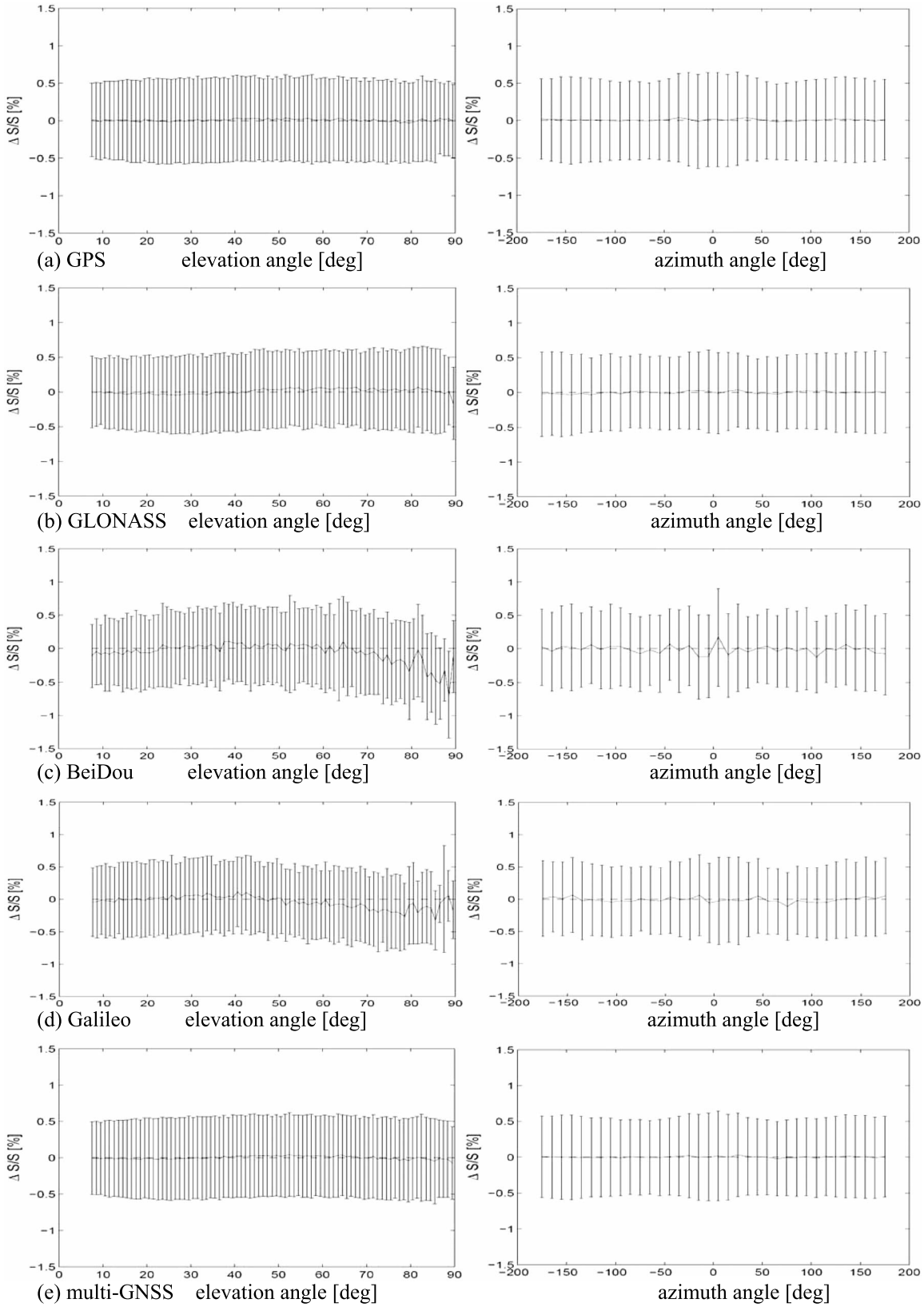

Figure 10. The fractional deviation between GNSS STDs and ECMWF STDs as a function of the (left column) elevation angle and (right column) azimuth angle (right). The black line indicates the mean fractional deviation, and the error bars indicate the standard fractional deviation from the mean deviation. Figures 10a–10e are for GPS, GLONASS, BeiDou, Galileo, and multi-GNSS combined STDs.

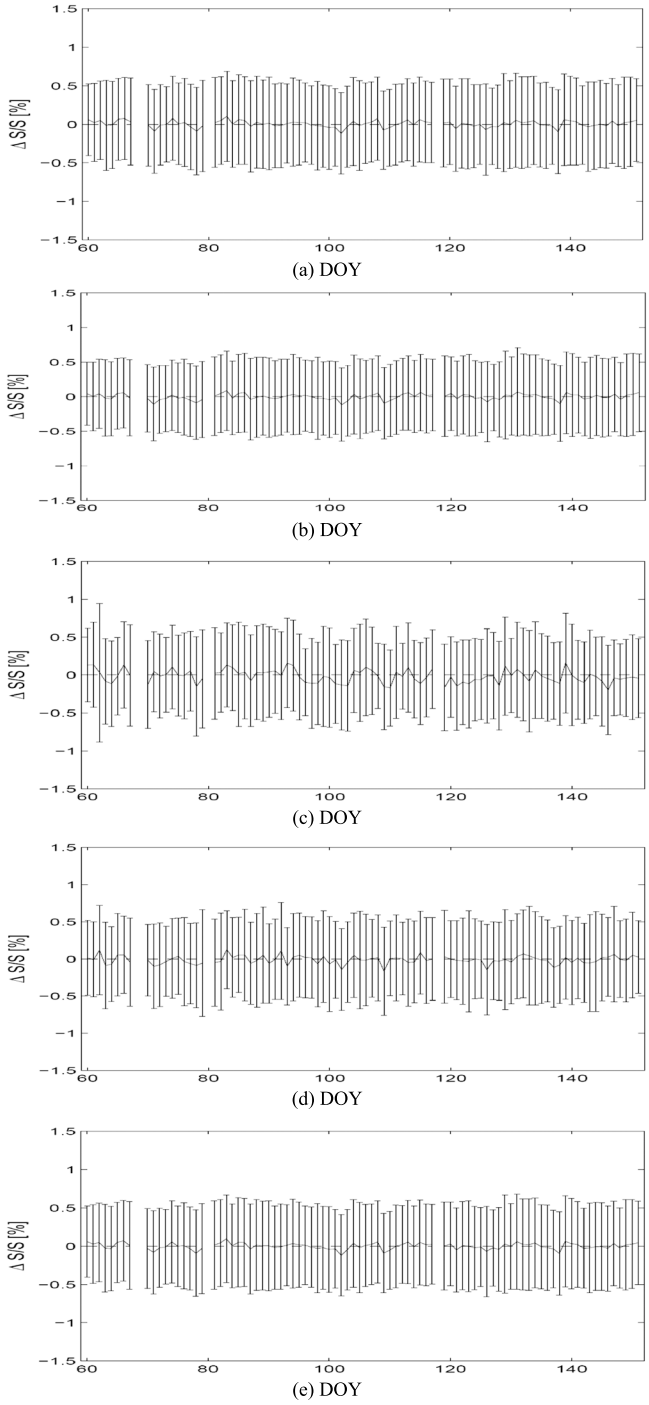

Figure 11. The fractional deviation between GNSS STDs and ECMWF STDs as a function of the day of year. The black line indicates the mean deviation, and the error bars indicate the standard deviation from the mean deviation. (a–e) GPS, GLONASS, BeiDou, Galileo, and multi-GNSS combined STDs.

elevation angels larger than 80°, 800 and 590 observations enter the statistics for BeiDou and Galileo respectively. Since GPS, GLONASS, Galileo and BeiDou share the same estimated ZWD (and horizontal delay gradients), we took a closer look on the post fit residuals, and indeed, we found that if post fit residuals for Galileo and BeiDou are discarded, the mean fractional deviation close to the zenith is zero. A possible reason is the precision of developed error models for the new satellite systems (e.g., the PCO and PCV models). The fractional standard deviation, indicated by the error bars, is stable for the entire elevation range and about 0.55%. In fact, the fractional standard deviation is slightly decreasing for decreasing elevation angles; for an elevation angle of 7° the standard deviation is about 0.5%. This can be also seen in the fractional deviation between GNSS and ECMWF STDs as a function of the azimuth angle: for azimuth angles around 0°, the elevation angles are typically close to zenith (in particular for the GPS, refer to the sky plot shown Figure 8), and thus, the fractional deviation is slightly larger. In essence, from the perspective of the NWM, the relative accuracy of low elevation GNSS STDs is higher than the relative accuracy of GNSS STDs close to the zenith.

The fractional deviation between GNSS and ECMWF STDs as a function of the day of year shown in Figure 11 indicates similar to Figure 6 the reliability of the individual and combined solutions. The increased variability in the fractional mean and standard deviation for BeiDou is attributed to the larger number of observations in low-latitude regions for which the deviations are larger in general (see Figure 6).

Figure 12 shows the map of station specific fractional mean and standard deviations. Similar to the mean and standard deviation of the ZTD (see Figure 6), the fractional deviations show a strong latitude dependence. In the tropics the mean fractional deviation reaches about 0.5% (with a nominal STD of 2.4 m close to zenith this translates into a mean deviation of 12 mm) and the fractional standard deviation reaches about 0.7% (with a nominal STD of 2.4 m close to zenith this translates into a

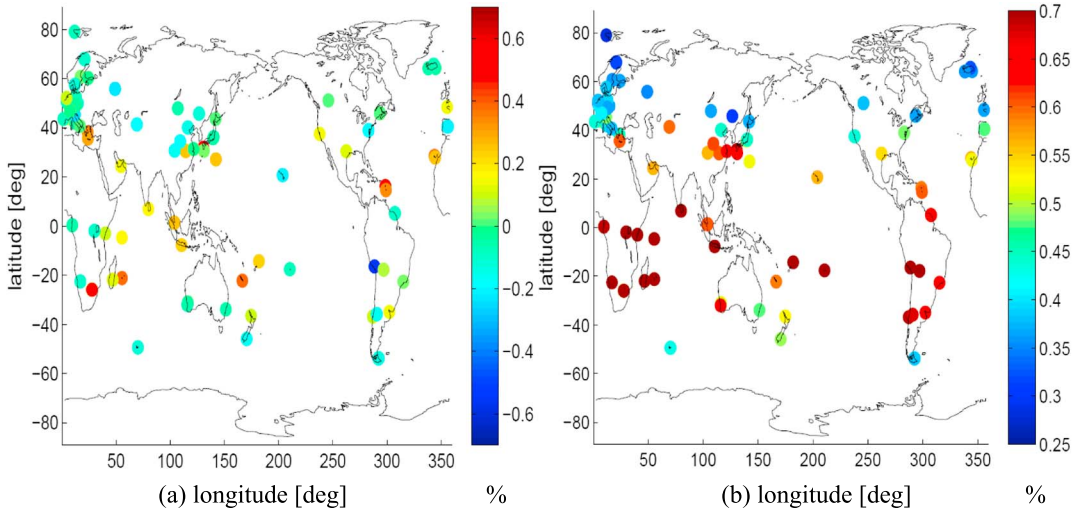

Figure 12. The fractional deviation between multi-GNSS STDs and ECMWF STDs for individual stations. (a) The mean deviation and (b) the standard deviation are presented.

standard deviation of 17 mm). For high-latitude stations the mean deviation is typically below 0.2% and the standard deviations are below 0.4%.

5. Conclusions

In this study, we developed a multi-GNSS processing, which makes full use of all available observations from different GNSS, for real-time atmospheric parameter retrieving. We processed the multi-GNSS observations of a 180 day period from about 100 globally distributed stations in both single-GNSS and multi-GNSS modes. The retrieved atmospheric parameters including ZTD, IWV, gradients, and STD derived are carefully analyzed and compared with those derived from WVR measurements and ECWMF data to independently evaluate the performance of individual GNSS and also to demonstrate the benefits of multiconstellation GNSS for real-time atmospheric monitoring.

The IWV comparisons with WVR show that the GLONASS-only solution is slightly worse than GPS-only solution and the RMS values for them are 1.8 and 1.6 mm, respectively. The BeiDou-only solution reveals largest RMS of about 2.5 mm; the RMS of the multi-GNSS combined solution is the smallest and about 1.2 mm. Although the GPS- and GLONASS-derived IWV are stable and have much less outliers than BeiDou-derived IWV, still some outliers can be identified. These outliers, appearing in single-system solutions, can be mitigated when multi-GNSS observations are processed simultaneous. From the comparisons, we can conclude that the GLONASS and BeiDou also have the potential capability for real-time IWV retrieval for time-critical meteorological applications such as NWP nowcasting and severe weather event monitoring. Moreover, the combination of multi-GNSS observations can improve the performance of single-system solution in meteorological applications with higher accuracy and robustness.

The ECMWF is used to evaluate the performance of the ZTDs, gradients, and STDs from multi-GNSS processing. Both ZTDs and gradients, derived from multi-GNSS, indicate good agreement with ECMWF estimates. The multi-GNSS processing greatly increases the number of STDs. The standard deviation between any GNSS and ECMWF STDs shows an elevation angle dependency, which is about 1 cm close to the zenith and about 10 cm at an elevation angle of 7°. The mean and standard fractional deviation between GNSS STDs and ECMWF STDs exhibit good stability as function of the elevation angle, the azimuth angle, and the time. Only BeiDou and Galileo STDs experience large mean fractional deviations of about several millimeter at high elevation angles above 70°. It may be caused by the residual errors in observation modeling of the new satellite systems. Both the mean and standard fractional deviations show a strong latitude dependence. In the tropics the mean fractional deviation reaches about 0.5% and the fractional standard deviation reaches about 0.7%. For high-latitude stations the mean deviation is typically below 0.2% and the standard deviations are below 0.4%.

These atmospheric parameters retrieved from multi-GNSS are very promising and have huge potential for meteorological applications, like improving short-term precipitation forecast or to provide an improved database for 3-D water vapor reconstructions [*Bender et al*., 2011]. The data assimilation of the multi-GNSS real-time atmospheric products into NWM for short-term forecast and nowcasting of strong precipitation events will be the focus of future work.

Acknowledgments
Thanks go to the International GNSS Service (IGS) for providing multi-GNSS data. The data are available at ftp://cddis.gsfc.nasa.gov/gnss/data/campaign/mgex/. We also want to thank Gunnar Elgered and Peter Forkman for the water vapor radiometer (WVR) data.

References

Al-Shaery, A., S. Zhang, and C. Rizos (2013), An enhanced calibration method of GLONASS inter-channel bias for GNSS RTK, *GPS Solutions*, *17*(2), 165–173.

Askne, J., and H. Nordius (1987), Estimation of tropospheric delay for microwaves from surface weather data, *Radio Sci.*, *22*, 379–386, doi:10.1029/RS022i003p00379.

Bender, M., R. Stosius, F. Zus, G. Dick, J. Wickert, and A. Raabe (2011), GNSS water vapour tomography—Expected improvements by combining GPS, GLONASS and Galileo observations, *Adv. Space Res.*, *47*(5), 886–897.

Bevis, M., S. Businger, T. Herring, C. Rocken, R. Anthes, and R. Ware (1992), GPS meteorology: Remote sensing of atmospheric water vapor using GPS, *J. Geophys. Res.*, *97*, 15,787–15,801, doi:10.1029/92JD01517.

Bevis, M., S. Businger, S. Chiswell, T. Herring, R. Anthes, C. Rocken, and R. Ware (1994), GPS meteorology: Mapping zenith wet delays onto precipitable water, *J. Appl. Meteorol.*, *33*, 379–386.

Böhm, J., A. Niell, P. Tregoning, and H. Schuh (2006), Global mapping function (GMF): A new empirical mapping function based on numerical weather model data, *Geophys. Res. Lett.*, *33*, L07304, doi:10.1029/2005GL025546.

Caissy, M., L. Agrotis, G. Weber, M. Hernandez-Pajares, and U. Hugentobler (2012), Coming soon: The International GNSS real-time service, *GPS World*, *23*(6), 52–58.

Dach, R., S. Schaer, and U. Hugentobler (2006), Combined multi-system GNSS analysis for time and frequency transfer, in *Proceedings of the European Frequency Time Forum*, pp. 530–537, IEEE, Braunschweig, Germany.

Dick, G., G. Gendt, and C. Reigber (2001), First experience with near real-time water vapor estimation in a German GPS network, *J. Atmos. Sol. Terr. Phys.*, *63*, 1295–1304.

Dousa, J., and G. V. Bennitt (2013), Estimation and evaluation of hourly updated global GPS zenith total delays over ten months, *GPS Solutions*, *17*(4), 453–464, doi:10.1007/s10291-012-0291-7.

Dousa, J., and P. Vaclavovic (2014), Real-time zenith tropospheric delays in support of numerical weather prediction applications, *Adv. Space Res.*, *53*(9), 1347–1358.

Elgered, G., and P. O. J. Jarlemark (1998), Ground-based microwave radiometry and long-term observations of atmospheric water vapor, *Radio Sci.*, *33*, 707–717, doi:10.1029/98RS00488.

Fang, P., M. Bevis, Y. Bock, S. Gutman, and D. Wolfe (1998), GPS meteorology: Reducing systematic errors in geodetic estimates for zenith delay, *Geophys. Res. Lett.*, *25*, 3583–3586, doi:10.1029/98GL02755.

Ge, M., H. Zhang, X. Jia, S. Song, and J. Wickert (2012), What is achievable with the current COMPASS constellation?, *GPS World*, *1*, 29–34.

Gendt, G., G. Dick, C. Reigber, M. Tomassini, Y. Liu, and M. Ramatschi (2004), Near real time GPS water vapor monitoring for numerical weather prediction in Germany, *J. Meteorol. Soc. Jpn.*, *82*, 361–370.

Gutman, S. I., S. R. Sahm, S. G. Benjamin, B. E. Schwartz, K. L. Holub, J. Q. Stewart, and T. L. Smith (2004), Rapid retrieval and assimilation of ground based GPS precipitable water observations at the NOAA Forecast Systems Laboratory: Impact on weather forecasts, *J. Meteorol. Soc. Jpn.*, *82*, 351–360.

Haan, S., S. Barlag, H. Baltink, and F. Debie (2004), Synergetic use of GPS water vapor and Meteosat images for synoptic weather forecasting, *J. Appl. Meteorol.*, *43*, 514–518.

Karabatic, A., R. Weber, and T. Haiden (2011), Near real-time estimation of tropospheric water vapour content from ground based GNSS data and its potential contribution to weather now-casting in Austria, *Adv. Space Res.*, *47*, 1691–1703.

Kouba, J. (2009), A guide to using International GNSS Service (IGS) products. [Available at http://igscb.jpl.nasa.gov/igscb/resource/pubs/UsingIGSProductsVer21.pdf.]

Lagler, K., M. Schindelegger, J. Böhm, H. Krásná, and T. Nilsson (2013), GPT2: Empirical slant delay model for radio space geodetic techniques, *Geophys. Res. Lett.*, *40*, 1069–1073, doi:10.1002/grl.50288.

Li, X., X. Zhang, and M. Ge (2011), Regional reference network augmented precise point positioning for instantaneous ambiguity resolution, *J. Geod.*, *85*, 151–158.

Li, X., M. Ge, H. Zhang, and J. Wickert (2013a), A method for improving uncalibrated phase delay estimation and ambiguity-fixing in real-time precise point positioning, *J. Geod.*, *87*(5), 405–416.

Li, X., M. Ge, X. Zhang, Y. Zhang, B. Guo, R. Wang, J. Klotz, and J. Wickert (2013b), Real-time high-rate co-seismic displacement from ambiguity-fixed precise point positioning: Application to earthquake early warning, *Geophys. Res. Lett.*, *40*, 295–300, doi:10.1002/grl.50138.

Li, X., G. Dick, M. Ge, S. Heise, J. Wickert, and M. Bender (2014), Real-time GPS sensing of atmospheric water vapor: Precise point positioning with orbit, clock and phase delay corrections, *Geophys. Res. Lett.*, *41*, 3615–3621, doi:10.1002/2013GL058721.

Li, X., X. Zhang, X. Ren, M. Fritsche, J. Wickert, and H. Schuh (2015a), Precise positioning with current multi-constellation Global Navigation Satellite Systems: GPS, GLONASS, Galileo and BeiDou, *Sci. Rep.*, *5*, 8328, doi:10.1038/srep08328.

Li, X., M. Ge, X. Dai, X. Ren, M. Fritsche, J. Wickert, and H. Schuh (2015b), Accuracy and reliability of multi-GNSS real-time precise positioning: GPS, GLONASS, BeiDou, and Galileo, *J. Geod.*, *89*(6), 607–635.

Li, X., F. Zus, C. Lu, T. Ning, G. Dick, M. Ge, J. Wickert, and H. Schuh (2015c), Retrieving high-resolution tropospheric gradients from multiconstellation GNSS observations, *Geophys. Res. Lett.*, *42*, 4173–4181, doi:10.1002/2015GL063856.

Mattioli, V., E. R. Westwater, S. I. Gutman, and V. R. Morris (2005), Forward model studies of water vapor using scanning microwave radiometers, Global Positioning System, and radiosondes during the Cloudiness Inter-Comparison Experiment, *IEEE Trans. Geosci. Remote Sens.*, *43*(5), 1012–1021.

Montenbruck, O., P. Steigenberger, R. Khachikyan, G. Weber, R. B. Langley, L. Mervart, and U. Hugentobler (2014), IGS-MGEX: Preparing the ground for multi-constellation GNSS science, *Inside GNSS*, *9*(1), 42–49.

Rizos, C., O. Montenbruck, R. Weber, R. Neilan, and U. Hugentobler (2013), The IGS MGEX Experiment as a Milestone for a Comprehensive Multi-GNSS Service ION-PNT-2013, Honolulu, 22–25 Apr.

Rocken, C., R. Ware, T. Van Hove, F. Solheim, C. Alber, and J. Johnson (1993), Sensing atmospheric water vapor with the Global Positioning System, *Geophys. Res. Lett.*, *20*, 2631–2634, doi:10.1029/93GL02935.

Rocken, C., T. Van Hove, and R. Ware (1997), Near real-time sensing of atmospheric water vapor, *Geophys. Res. Lett.*, *24*, 3221–3224, doi:10.1029/97GL03312.

Saastamoinen, J. (1973), Contributions to the theory of atmospheric refraction – Part II. Refraction corrections in satellite geodesy, *Bull. Géod.*, *47*(1), 13–34, doi:10.1007/BF02522083.

Shoji, Y., M. Kunii, and K. Saito (2011), Mesoscale data assimilation of Myanmar cyclone Nargis Part II: Assimilation of GPS-derived precipitable water vapor, *J. Meteorol. Soc. Jpn.*, *89*, 67–88.

Wang, J., L. Zhang, and A. Dai (2005), Global estimates of water-vapor-weighted mean temperature of the atmosphere for GPS applications, *J. Geophys. Res.*, *110*, D21101, doi:10.1029/2005JD006215.

Ware, R., C. Alber, C. Rocken, and F. Solheim (1997), Sensing integrated water vapor along GPS ray paths, *Geophys. Res. Lett.*, *24*, 417–420, doi:10.1029/97GL00080.

Yuan, Y., K. Zhang, W. Rohm, S. Choy, R. Norman, and C. S. Wang (2014), Real-time retrieval of precipitable water vapor from GPS precise point positioning, *J. Geophys. Res. Atmos.*, *119*, 10,044–10,057.

Zhang, X., X. Li, and F. Guo (2012), Satellite clock estimation at 1 Hz for realtime kinematic PPP applications, *GPS Solutions*, *15*(4), 315–324, doi:10.1007/s10291-010-0191-7.

Zumberge, J. F., M. B. Heflin, D. C. Jefferson, M. M. Watkins, and F. H. Webb (1997), Precise point positioning for the efficient and robust analysis of GPS data from large networks, *J. Geophys. Res.*, *102*, 5005–5017, doi:10.1029/96JB03860.

Zus, F., M. Bender, Z. Deng, G. Dick, S. Heise, M. Shang-Guan, and J. Wickert (2012), A methodology to compute GPS slant total delays in a numerical weather model, *Radio Sci.*, *47*, RS2018, doi:10.1029/2011RS004853.

Zus, F., G. Dick, J. Dousa, S. Heise, and J. Wickert (2014), The rapid and precise computation of GPS slant total delays and mapping factors utilizing a numerical weather model, *Radio Sci.*, *49*, 207–216, doi:10.1002/2013RS005280.

Zus, F., G. Dick, S. Heise, and J. Wickert (2015), A forward operator and its adjoint for GPS slant total delays, *Radio Sci.*, *50*, 393–405, doi:10.1002/2014RS005584.